Ka-Band Huygens Antenna Arrays with Very High Aperture Efficiency and Low Sidelobes

Wei Lin, *Senior Member, IEEE* and Richard W. Ziolkowski, *Life Fellow, IEEE*

***Abstract*—A *Ka*-band Huygens antenna array with extremely high aperture efficiency and low sidelobe levels is reported for 5G millimeter-wave wireless applications. The basic array element is an innovative Huygens sub-array consisting of two open rectangular waveguides that form an aperture consisting of a 1×2 set of orthogonal, tightly-coupled electric and magnetic elements separated by a virtual gap that are balanced, in-phase and radiate Huygens cardioid patterns. A larger 8×16 element array is then realized with 64 of these 1×2 sub-arrays. With excitations of equal amplitude, the full broadside-radiating array achieves an aperture efficiency up to 97.5% in the operating bandwidth, which is very close to the 100% limit associated with an ideal uniform aperture distribution. Moreover, a highly-efficient and compact feed network with tapered-amplitude and in-phase excitations from the array center to its edges is designed to achieve sidelobe and backlobe levels less than –20 dB. The –10 dB impedance bandwidth covers 26.7 to 29.65 GHz and the peak realized aperture efficiency reaches 82%. A full-aluminum array prototype was fabricated with standard machining processes and tested. The measured performance characteristics agree well with their simulated values, confirming the efficacy of their designs.**

***Index Terms*—5G wireless systems, antenna arrays, aperture efficiency, complementary sources, Huygens antennas, *Ka*-band, sidelobe levels, millimeter-wave.**

I. INTRODUCTION

Aperture efficiency (AE) is one of the critical antenna array characteristics that determines the maximum achievable directivity if the physical area of an array is given [1]. It characterizes how effectively the antenna array utilizes the input power. High aperture efficiency is especially important for arrays operating at higher frequency bands, e.g., the millimeter-wave band, because the associated path losses of electromagnetic waves in air significantly increase when the operating frequency increases [2]. Another critical array parameter is the sidelobe level in its radiation patterns. High sidelobes can increase the noise level in a receiver [3] as well as cause unwanted signal interference [4]. For instance, radar systems require all sidelobe levels to be less than -20 dB [5]. However, it is very challenging for an antenna array to achieve both high aperture efficiency and low sidelobe levels simultaneously, particularly with *Ka* band (26.5 to 40 GHz) millimeter-wave antenna arrays [6] – [8]. The losses associated with both their feed networks and radiating elements are commonly higher in comparison to their lower frequency counterparts.

One design methodology to achieve low sidelobes relative to the main beam of an antenna array is to employ amplitude-tapered excitations of its radiating elements. Many antenna arrays with sidelobe levels below –20 dB have been developed. Typical examples are found in the reported works [9] – [18]. They were realized with a variety of configurations including microstrip patch arrays with tapered feed networks [9], [10]; series-fed patch arrays [11], [12]; complementary split-ring resonator (CSRR) loaded patch arrays [13]; slot arrays [14], [15]; leaky-wave arrays [16]; metasurface antenna arrays [17], and a $TE_{0.5,0}$ mode waveguide-based Huygens array [18].

Manuscript received xx, 2022; This work was supported by the Australia Research Council Discovery Early Career Researcher Award under Grant PRO20-9959. The authors are with the Global Big Data Technologies Centre, School of Electrical and Data Engineering, University of Technology Sydney, Ultimo, NSW 2007, Australia (email: Wei.Lin@uts.edu.au; Richard.Ziolkowski@uts.edu.au)

The highest peak realized aperture efficiency among these works is 67% in [18]. Note that we adopt the realized aperture efficiency (RAE) figure-of-merit that was defined in [18] to make fair comparisons among all of the related references in this paper. The RAE takes into consideration all of the losses associated with the antenna array; and thus, it better characterizes how effectively an antenna not only utilizes its physical aperture, but also how well it radiates.

In this paper, we report the development of a *Ka*-band Huygens antenna arrays with 8×16 elements that simultaneously achieves both high realized aperture efficiency and low sidelobes. In comparison to the aforementioned arrays, the RAE achieved in this work is improved significantly. It is the first realized *Ka*-band low sidelobe array with all sidelobes and backlobes being less than –20 dB that achieves a peak RAE over 80%. Furthermore, it is the first reported large-scale antenna array that achieves an AE close to 100% (97.5%) under equal-amplitude excitations. The basic radiating element of the entire array is an innovative 1×2 Huygens sub-array which consists of two rectangular open waveguides with only one waveguide-port excitation that form an aperture composed of a 1×2 set of orthogonal, tightly-coupled electric and magnetic elements separated by a virtual gap which are balanced, in-phase and consequently radiate Huygens cardioid patterns. It is a simple structure and is machined as an all-metal block. A larger 8×16 element array is then realized with 64 of these basic 1×2 sub-arrays. The entire aperture size is 80 mm × 80 mm (~7.5 λ_f × 7.5 λ_f at f = 28 GHz). To achieve the low, less than –20 dB sidelobe levels, an efficient waveguide feed network with tapered-amplitude and in-phase excitations from the center to the edges of the array is designed. The –10 dB impedance bandwidth covers 26.7 to 29.65 GHz (10.47%) in the *Ka*-band. As designed, it is demonstrated that all of the sidelobe and backlobe levels are less than –20 dB within the bandwidth. It is an ideal candidate for 5G millimeter-wave (mm-wave) wireless applications that require high AE and RAE values and very low sidelobe levels.

II. FULL-METAL 1 × 2 HUYGENS SUB-ARRAY WITH RECTANGULAR WAVEGUIDE EXCITATIONS

The configuration of the all-metal 1×2 Huygens sub-array is shown in Fig. 1. The entire structure is realized with a single metal block with internal cavities. Aluminum with its relative permittivity, permeability and conductivity being 1.0, 1.0, and 3.8×10^7 Siemens/m, respectively, is chosen for our all-metal design to facilitate its fabrication. Fig. 1(a) shows a perspective view of the entire sub-array; Figs. 1(b) and 1(c) highlight its internal waveguide structures with, respectively, a perspective bottom view and a front view.

The sub-array consists of two rectangular open waveguides (WG#1 and WG#2), two pairs of tightly-coupled dipoles (Dipole#1 and Dipole#2), two current chokes, and a Y-shaped E-plane (*yz*-plane) waveguide power divider. The magnetic radiators are formed on the openings of the two waveguides, and the electric radiators are produced by the dipole arms that are the plates extended laterally from the waveguide openings. A virtual gap is realized between the two dipole arms, i.e., there is no physical gap in the aperture of the structure. This is facilitated by the design because the electrical length of the Huygens source is dominated by the depth of the waveguide cavities. The virtual gap design concept is very important because it facilitates

achieving the highest possible aperture efficiency, i.e., it allows the entire surface of the aperture to be utilized very effectively, as well as its single metal block construction. Orthogonal and in-phase radiators are realized in this manner. Although the 1×2 sub-array appears to contain only two pairs of Huygens elements, the directivity it achieves is close to that of an equivalent four element 2×2 ideal Huygens dipole antenna array (HDAA) according to the analysis developed in [20].

The two current chokes below and parallel to the electric radiators have the same size as the dipole arms; they eliminate the currents flowing downward along the outside walls of the metal block. The two open waveguides are excited via the narrow slots on the bottom that are cascaded to the power divider formed by the Y-shaped metal waveguide block beneath them. The bottom of the entire sub-array is a (single) waveguide port. Three sets of matching blocks are placed inside the power divider. This configuration greatly eased the fabrication of the expanded large scale 8×16 element array.

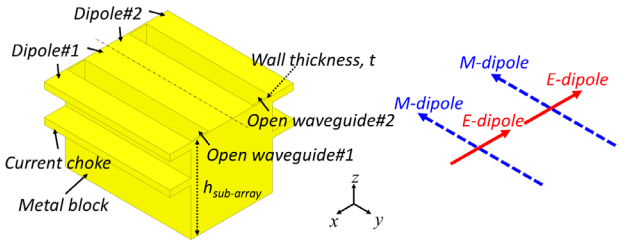

(a) All metal 1×2 sub-array and its effective Huygens elements

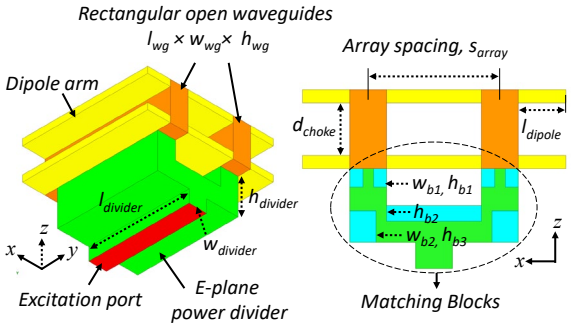

(b) Internal structures (c) Front view of internal structures

Fig. 1. Configuration of the Huygens sub-array. (a) Perspective view of the entire full metal sub-array. (b) Perspective view of the internal structures inside the metal enclosure. (c) Front view of the internal structures.

The design is targeted for *Ka*-band applications and was optimized at 28 GHz band for 5G wireless systems. The detailed parameters of the sub-array are (dimensions in millimeters): l_{wg} = 10.0, w_{wg} = 1.4, h_{wg} = 3.0, $l_{divider}$ = 8.0, $w_{divider}$ = 1.4, $h_{divider}$ = 2.8, t = 0.05, s_{array} = 5.0, d_{choke} = 2.0, l_{dipole} = 1.8, w_{b1} = 0.5, h_{b1} = 0.7, h_{b1} = 0.6, w_{b2} = 1.0, h_{b3} = 1.2.

A. Huygens operating principles and performance

The electric and magnetic radiators formed by the entire top surface of the sub-array, its aperture, meet the conditions that realize the balanced condition of a Huygens source, i.e., these elements form two balanced pairs of orthogonal and in-phase E- and M-dipole radiators [19], [20]. The analogous complementary-source-based concept has been extensively studied in many magnetoelectric (ME) dipole antenna papers, e.g., [21], [22]. Fig. 2 and Fig. 3 present the electric-field magnitude distributions on the array's top surfaces of the two dipole plates and the magnetic-field magnitude distributions inside its waveguides at 28 GHz for four times separated by a quarter of the period, *T*, at 28 GHz. It is clearly observed that the electric and magnetic fields are resonating in time alternately over each quarter period.

The closely coupled pair of open waveguides operate in their TE_{10} mode. This aspect is fundamentally different from the SIW-based waveguides in [18] that operate in their $TE_{0.5,0}$ mode. The electric field amplitudes across the waveguide opening are explicitly depicted in Fig. 2(a), i.e., they are along the +*x*-direction at t = 3T/4 and along the -*x*-direction at t = T/4. As indicated in Fig. 2(b), the distance from the excitation port to the opening is h_{wg}. To guarantee the maximum magnetic fields occur with the requisite phase over their openings, the depth of these was initially set so that a quarter-wave propagation, i.e., $k_z \times h_{wg} = \pi/2$, occurs, where the wave number along z for the TE_{10} mode is [23]:

$$k_z = \sqrt{(\omega/c)^2 - (\pi/l_{wg})^2} = \frac{2\pi}{\lambda_0}\sqrt{\varepsilon_r - \left(\frac{\lambda_0}{2\,l_{wg}}\right)^2} \qquad (1)$$

$c = 1/\sqrt{\varepsilon_0\mu_0}$ being the speed of light, λ_0 the free-space wavelength, and the transverse wavenumbers $k_x = \pi/w_{wg}$ and $k_y = \pi/l_{wg}$.

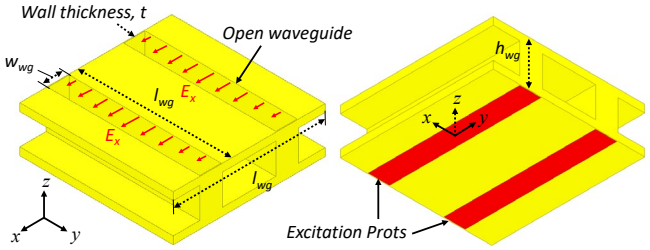

Fig. 2. Configuration of the top radiating elements of the sub-array without the power divider. (a) Perspective view. (b) Bottom view.

The electric and magnetic field distributions and the associated equivalent currents in the waveguides and on the dipole plates are illustrated in Fig. 3 at quarter-period time intervals at 28 GHz. The currents on the dipole plates are along the –*x*-direction when t = 0 as indicated in the corresponding top sub-plot. The magnetic fields on the interior walls of the metallic waveguide shown in Fig. 3 arise from the electric currents along the z-direction, i.e., $\vec{J}_s(x = \pm w_{wg}/2) = \mp\hat{x} \times H_y\hat{y} = \mp H_y\,\hat{z}$, but they are 90º behind the electric field ones. Thus, they correspond to the current arrows indicated in the t = 3T/ 4 lower sub-plot. Similarly, because the electric field is orthogonal to the long edges of the waveguide openings, the equivalent magnetic currents $\vec{K}_s = -\hat{z} \times E_{wg,op}\,\hat{x}$ at t = 0 are along the -*y*-direction as depicted in the corresponding bottom sub-plot. Consequently, these effective electric and magnetic currents are orthogonal to each other and their cross product $\vec{J}_s \times \vec{K}_s$ is along the +*z*-direction, i.e., $-\hat{x} \times -\hat{y} = \hat{z}$. Moreover, with the 90° phase difference of these current elements, the fields they radiate are in-phase [1]. These are the necessary conditions to ensure the radiated fields have Huygens cardioid patterns. The actual balance of the amplitudes of the E- and M-radiators are adjusted by changing the waveguide width as will be demonstrated in the next subsection. Note that the field distributions in Fig. 3 also confirm the formation of the virtual gap between the two dipoles.

Fig. 4 (a) shows the simulated results of the $|S_{11}|$, directivity and realized gain values of the sub-array as functions of the source frequency. The minimum $|S_{11}|$ value is at 28 GHz. The –10 dB impedance bandwidth covers 25.8 to 30 GHz, a 15% fractional bandwidth. Very high directivity and realized gain values are observed.

The latter are stable within the bandwidth. In particular, the directivity and realized gain values at 28 GHz are 10.46 dBi and 10.32 dBi, respectively. The 0.14 dB drop in the realized gain is due to the metal losses and small impedance mismatch. Fig. 4 (b) shows the normalized radiation patterns at 28 GHz. The front-to-back-ratio is large, 17 dB, without a ground plane being present. These results further confirm that the sub-array operates according to the Huygens principles.

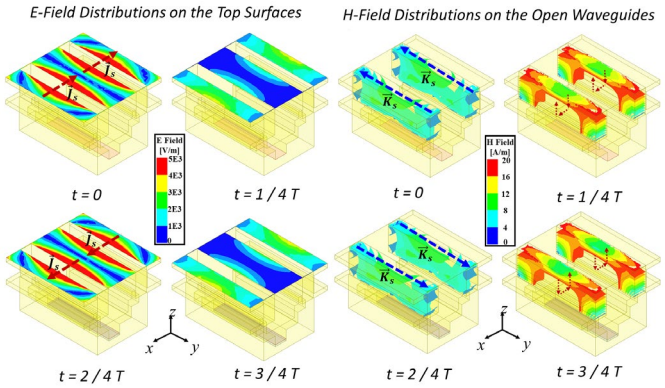

Fig. 3. Electric-field magnitude distributions on the top surfaces of the Huygens sub-array and magnetic-field magnitude distributions inside the rectangular open waveguide in a period of time, T, at 28 GHz.

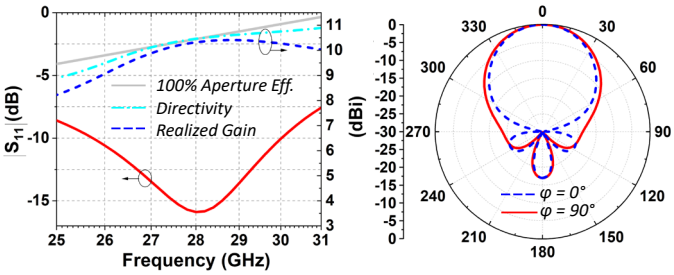

Fig. 4. Simulated results of the 1×2 Huygens sub-array. (a) $|S_{11}|$, directivity and realized gain values as functions of the source frequency when the area of the sub-array aperture is 10 mm × 10 mm ($\lambda_{f=30GHz} \times \lambda_{f=30GHz}$). (b) Normalized radiation patterns of the sub-array at 28 GHz.

It was noted in [24] that the definition of AE for an antenna array is only applicable for large scale arrays, not an array with only a few elements. Nevertheless, we use the AE and RAE definitions to calculate their values for the 1×2 sub-array. It is found that AE=100% and RAE=97% at 28 GHz. These values anticipate the very high aperture efficiency that will be demonstrated for the large scale 8×16 element array developed in the next section which is formed with 64 of these 1×2 sub-arrays.

B. Key design considerations to achieve the highest aperture efficiency

Proper designs of the open waveguides operating in their TE_{10} modes and of their extended dipole plates are essential for achieving the maximum directivity and realized gain. The initial value l_{wg} of our sub-array was set equal to 10.7 mm (1 λ at 28 GHz). Then, according to (1) and the desired propagation distance, $k_z \times h_{wg} = \pi/2$, is obtained with h_{wg} = 3.09 mm for our targeted 28 GHz. The final numerically optimized values l_{wg} and h_{wg} were 10.0 mm and 3.0 mm, respectively.

The width of the waveguide opening, w_{wg}, is critical to achieve the maximum directivity and, thus, the highest aperture efficiency because it not only determines the radiation resistance of the sub-array, but it also controls the balance between the amplitudes of the electric and magnetic radiators. Because of its all-metal realization, the value of w_{wg} is flexible. This design freedom is basically absent in PCB-based arrays such as those reported in [18]. When the total size of the square aperture ($l_{wg} \times l_{wg}$) of the entire sub-array is fixed, the opening width, w_{wg}, determines how much area the electric dipoles and magnetic openings will occupy, respectively, and thus, controls the amplitudes of E- and M-radiators. Fig. 5(a) shows the radiation resistance values of Port#1 and Port#2 as functions of the source frequency when the width of the waveguide opening is 0.4, 1.4, and 2.4 mm, respectively. The length of the waveguide that is also the side length of the square array aperture, l_{wg}, is fixed at 10 mm. It is clearly seen that the radiation resistance is very small if the width of the opening is too narrow (0.4 mm) and increases dramatically by enlarging it.

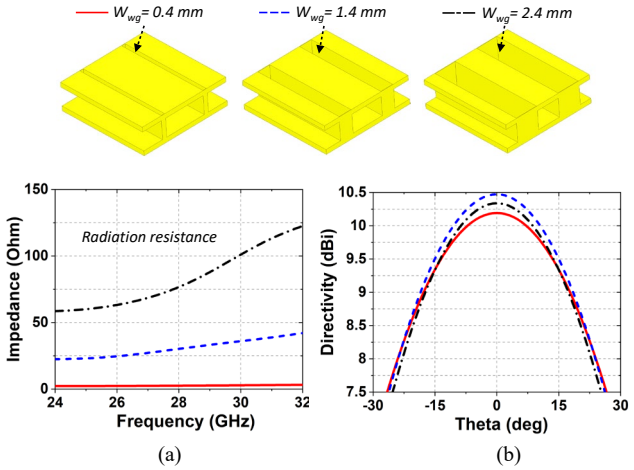

Fig. 5. Effects of the width of the open waveguide, when w_{wg}, is 0.4 mm, 1.4 mm and 2.4 mm, respectively. (a) Radiation resistance values as functions of the source frequency. (b) Directivity patterns at 28 GHz.

Impedance matching becomes much easier if the opening is wide, but the optimal value is also determined by the highest achievable RAE. Fig. 5(b) presents the directivity values of the sub-array for the same sets of opening width variations from 0.4 to 2.4 mm. Port#1 and Port#2 are excited with in-phase and equal amplitude sources. The directivity value reaches the maximum when the width, $w_{aperture}$, is 1.4 mm because more balanced fields are radiated by the equivalent electric and magnetic current elements in comparison to the other two structures, i.e., the best Huygens performance was attained. These results also confirm that our Huygens array, which includes both electric and magnetic radiators, is more directive than arrays of the same size formed with only single types of radiating elements, e.g., as dipole or slot arrays. Moreover, the aperture area is very efficiently utilized for broadside co-polarized radiation. 100% of the aperture area contributes to the broadside radiation if the thickness of the waveguide wall is neglected, e.g., wt = 0.

III. High Aperture Efficiency 8×16 Element Huygens Array with Ideal Excitations

To validate the high RAE performance of our design, a large scale 8×16 element array with ideal excitations that is based on the developed 1×2 sub-arrays as its basic elements is developed. They facilitate a careful evaluation of the AE performance of the final optimized design. It is demonstrated that outstanding AE values, close to 90%, are realized with tapered amplitudes and in-phase excitations. The desired low sidelobe levels, i.e., the target of less than –20 dB values, are achieved. Moreover, AE values nearly reaching 100% are realized when the array is under uniform excitations. To the best of our knowledge, these AE values are the highest among the large-scale

arrays reported to date.

The commonly employed tapered-amplitude, in-phase excitations are adopted to achieve the desired low sidelobe levels. The optimized weighting coefficients for each port to achieve sidelobe levels less than –20 dB are adopted. From the center axes of the array to its edges, the coefficients for each port are relatively 1.0, 0.75, 0.45, and 0.3, respectively. Fig. 6 shows the array's simulated normalized radiation patterns in both vertical principal planes, $\varphi = 0°$ and $\varphi = 90°$, at 27, 28 and 29 GHz. It is immediately observed that within the frequency range from 27 to 29 GHz, all sidelobe levels are less than –20 dB as desired.

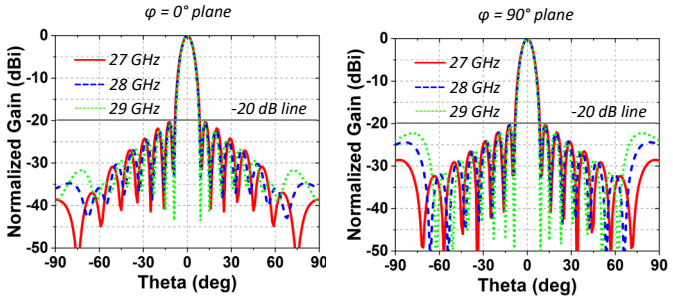

(a) (b)

Fig. 6. Normalized radiation patterns of the 8×16 element Huygens array at 27, 28 and 29 GHz in the two vertical principal planes: (a) $\varphi = 0°$, and (b) $\varphi = 90°$.

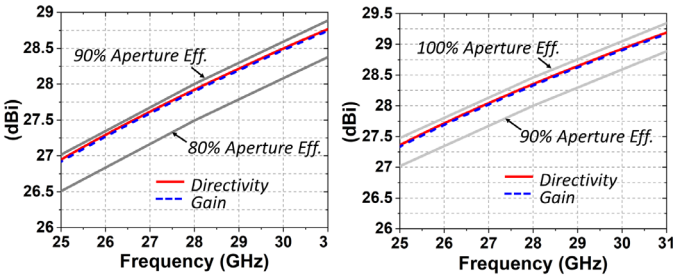

(a) (b)

Fig. 7. Directivity and gain values of the 8×16 element Huygens array as functions of the source frequency. (a) Tapered excitations. (b) Uniform excitations.

Moreover, high AE values are also realized. The directivity and gain values as functions of the source frequency are shown in Fig. 7 (a). The 90% and 80% AE curves are highlighted. The directivity and gain values at 28 GHz are 27.92 dBi and 27.9 dBi, respectively. The corresponding AE value is 88.3% and the radiation efficiency is 99%. Notably, it is the highest reported aperture efficiency for a large scale array whose sidelobe levels are all less than -20 dB. Furthermore, as seen in Fig. 7(b) in which the 100% and 90% AE curves are highlighted, close to 100% AE is achieved if the array elements are excited uniformly (i.e., equal amplitude and phase). Specifically, the directivity and gain values at 28 GHz are 28.35 dBi and 28.33 dBi, respectively. The corresponding AE value is 97.5%, and the radiation efficiency is 99%.

To the best of our knowledge, the achieved AE values, i.e., higher than 95%, are the highest among previously reported large-scale arrays. As concluded in [23], the maximum aperture efficiency, 100%, can only be achieved if an absolutely uniform distribution is realized over the entire aperture. Our Huygens array has almost reached this maximum AE limit.

The electric and magnetic field distributions on the aperture of the array are shown in Fig. 8 at quarter-periods in time. The tapering of the field magnitudes from its center to its edges is clearly observed.

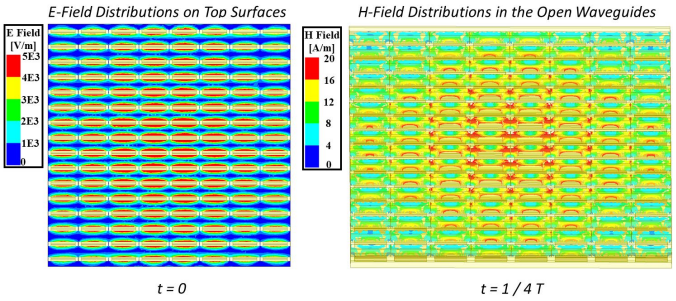

Fig. 8. Electric-field magnitude distributions on the top surfaces (front view) of the 8 × 16 Huygens array with low sidelobes, and magnetic-field magnitude distributions inside the open waveguides (perspective view to see into the waveguides) at quarter periods in time for the period, *T*, at 28 GHz.

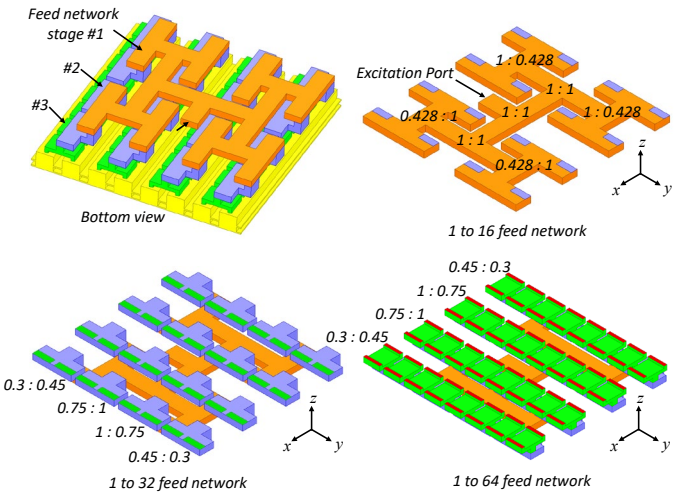

Fig. 9. Detailed descriptions of the feed networks with tapered outputs to realize the weighted excitations required for the low sidelobe 8 × 16 Huygens array.

IV. Unequal-Output Waveguide Feed Network Design

The design of the unequal-output waveguide feed network that achieves the tapered weighting coefficients was another major step in realizing the 8 × 16 Huygens array as an all-metal structure. The three-stage1-to-64 waveguide feed network shown in Fig. 9 was designed. Each layer and the assembled network on the array are displayed. It consists of three types of power dividers that are shown in Fig. 10. Fig. 10(a) depicts the H-plane power divider with its E-plane outputs. The cross section of the power divider is aligned with the H-field and the surface of the output port is aligned with the E-field. Fig. 10(b) depicts the H-plane power divider with the H-plane outputs. The surface of the output port is aligned with the H-field. Fig. 10(c) presents the E-plane power divider with the E-plane outputs. The cross section of the power divider is aligned with the E-field and the surface of the output port is also aligned with the E-field.

The bottom stage#1 is a 1-to-16 feed network that consists of three 1:1 (–3 dB : –3 dB) power ratio, four 0.428 : 1 (–5.2 dB : –1.55 dB) power ratio H-plane power dividers with E-plane outputs, and eight 0.428:1 (–5.2 dB : –1.55 dB) power ratio H-plane power dividers with H-plane outputs. The 16 H-plane outputs of stage#1 connect to stage#2. The latter is formed by the eight 0.75 : 1 (-3.67 dB : -2.43 dB) power ratio and eight 0.3 : 0.45 (-4 dB : -2.22 dB) power ratio H-plane power dividers with H-plane outputs. The 32 H-plane ports further connect to sixteen 0.75:1 (–3.67 dB : –2.43 dB) power ratio and sixteen 0.3:0.45 (–4 dB : –2.22 dB) power ratio E-plane power dividers with E-plane outputs in stage#3. The final 64 E-plane ports connect to the input ports

of the 64 1×2 sub-arrays that constitute the 8×16 element Huygens array.

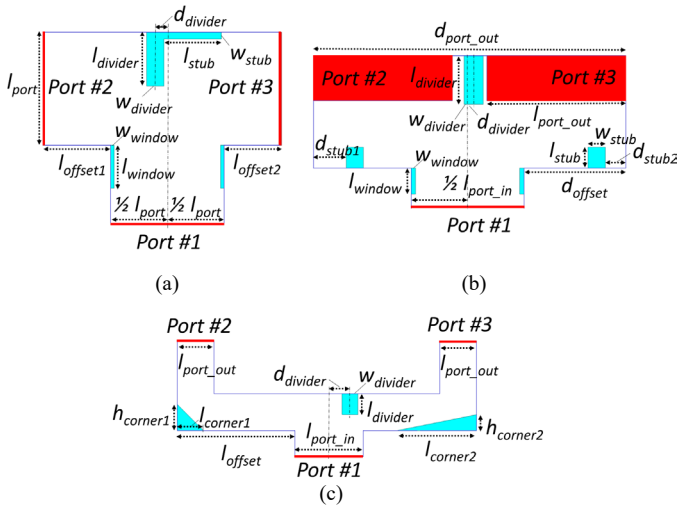

Fig. 10. Three types of waveguide power dividers are used to build the entire feed network. (a) H-plane power divider with E-plane outputs. (b) H-plane power divider with H-plane outputs. (c) E-plane power divider with E-plane outputs.

The detailed parameters of these power dividers are (in millimeters):

(a) H-plane power dividers with E-plane outputs. Parameters for the 1:1 or –3 dB : –3 dB power ratio are: l_{port} = 6.5, $l_{offset1}$ = 3.5, $l_{offset2}$ = 3.5, l_{window} = 2.5, w_{window} = 0.2, $l_{divider}$ = 3.1, $w_{divider}$ = 1.0, $d_{divider}$ =0, l_{stub} = 0, w_{stub} = 0. Parameters for the 0.428 : 1 or –5.2 dB : –1.55 dB power ratio are: l_{port} = 6.5, $l_{offset1}$ = 3.83, $l_{offset2}$ = 3.17, l_{window} = 2.5, w_{window} = 0.2, $l_{divider}$ = 3.1, $w_{divider}$ = 1.0, $d_{divider}$ = 0.55, l_{stub} = 3.3, w_{stub} = 0.4.

(b) H-plane power dividers with H-plane outputs. Parameters for the 1 : 0.75 or -2.43 dB : -3.67 dB power ratio are: l_{port_in} = 6.5, l_{port_out} = 8.0, d_{port_out} = 18.0, d_{offset} = 5.87, d_{stub1} = 1.875, d_{stub2} = 1.475, l_{window} = 1.5, w_{window} = 0.25, $l_{divider}$ = 2.8, $w_{divider}$ = 1.1, $d_{divider}$ = 0.25, l_{stub} = 1.2, w_{stub} = 1.0. Parameters for the 0.45 : 0.3 or -2.22 dB : -4 dB power ratio are: l_{port_in} = 6.5, l_{port_out} = 8.0, d_{port_out} = 18.0, d_{offset} = 5.87, d_{stub1} = 1.875, d_{stub2} = 1.175, l_{window} = 1.5, w_{window} = 0.35, $l_{divider}$ = 2.8, $w_{divider}$ = 1.1, $d_{divider}$ = 0.25, l_{stub} = 1.2, w_{stub} = 1.0.

(c) E-plane power dividers with E-plane outputs. Parameters for the 1 : 0.75 or -2.43 dB : -3.67 dB power ratio are l_{port_in} = 2.6, l_{port_out} = 1.4, l_{offset} = 4.48, $l_{corner1}$ = 1.0, $l_{corner2}$ = 2.7, $h_{corner1}$ = 1.0, $h_{corner2}$ = 0.6, $l_{divider}$ = 0.8, $w_{divider}$ = 0.6, $d_{divider}$ = 0.6. Parameters for the 0.45 : 0.3 or -2.22 dB : -4 dB power ratio are l_{port_in} = 2.6, l_{port_out} = 1.4, l_{offset} = 4.48, $l_{corner1}$ = 1.0, $l_{corner2}$ = 3.0, $h_{corner1}$ = 1.0, $h_{corner2}$ = 0.6, $l_{divider}$ = 0.8, $w_{divider}$ = 0.6, $d_{divider}$ = 0.8.

V. Measurement Results

The entire 8×16 array was fabricated with standard machining processes. They were accomplished by dividing the prototype's design into five separate aluminum plates, as shown in Fig. 11, which were machined separately and then joined together with screws. The total aperture size of the array is 80 mm × 80 mm (7.48 λ_c × 7.48 λ_c) and its height is 20 mm (1.87 λ_c). Photos of the assembled prototype array are shown in Fig. 12. The array is excited by a standard WR34 waveguide with the port connection on its bottom. Because it has much lower losses than PCB-based structures such as those in [18] do, its all-metal design is more suitable for higher frequency operations, e.g., for *Ka*-band mm-wave applications. Moreover, it is physically more robust and suitable for applications in harsh environments, e.g., in space.

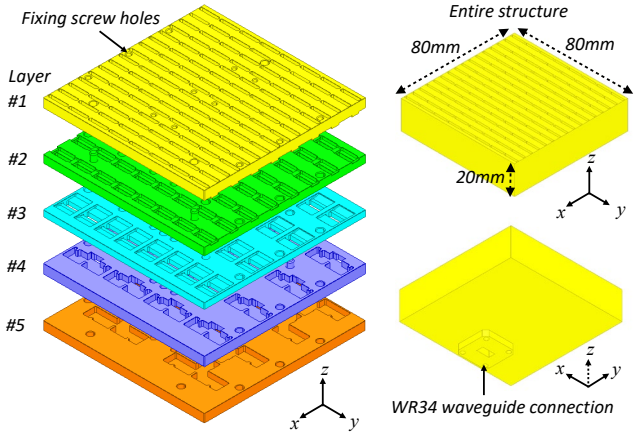

Fig. 11. Layered view of the fabricated prototype which was realized with five separate machined aluminum plates joined with screws.

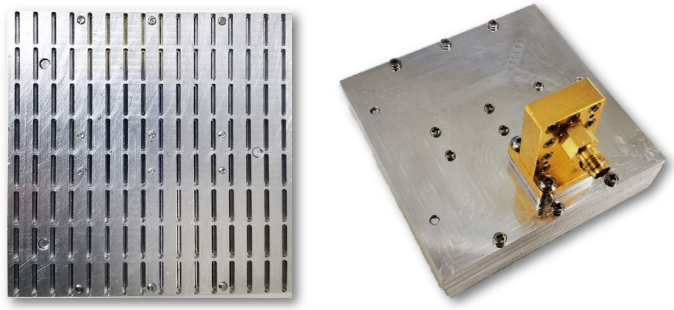

(a) (b)

Fig. 12. Assembled prototype. (a) Front view. (b) Bottom view with the WR34 waveguide to SMA adapter mounted.

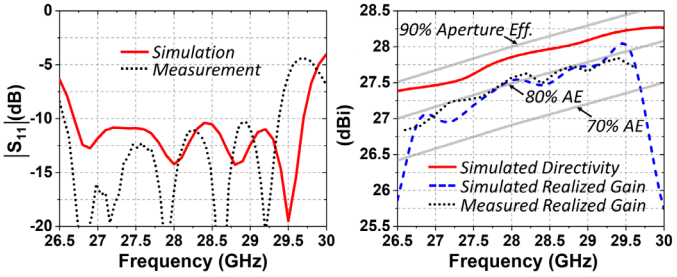

(a) (b)

Fig. 13. Measured and simulated performance characteristics as functions of the source frequency. (a) $|S_{11}|$. (b) Realized gain and directivity.

The simulated and measured $|S_{11}|$ values as functions of the source frequency are shown in Fig. 13(a). They agree reasonably well. The simulated (measured) –10-dB impedance bandwidth is 10.5% (10.0%), covering 26.7 to 29.65 GHz (26.55 to 29.35 GHz). The simulated realized gain and directivity values and the measured realized gain values are shown in Fig. 13(b) as functions of the source frequency. The simulated and measured realized gain values also agree reasonably well; the peak values being 28.03 dBi (simulated) and 27.84 dBi (measured). The simulated and measured peak RAE values are 82% and 81.4%, respectively. Note that the wall thickness between adjacent waveguides became 0.8 mm in the prototype to ensure the fabrication accuracy. The RAE would have been larger if the thickness of those walls had been smaller, which could be facilitated, for instance, by using more advanced fabrication processes.

The simulated and measured normalized realized gain patterns in the two principle vertical planes (φ = 0° and φ = 90°) at 28 GHz are shown in Fig. 14. The simulated and measured results again agree reasonably

well. All of the measured sidelobe and broadside cross-polarization levels are less than –20 dB and –30 dB, respectively. Note that simulated cross-polarization levels are below the scale used for these figures. All sidelobe levels are less than -20 dB across the entire frequency band.

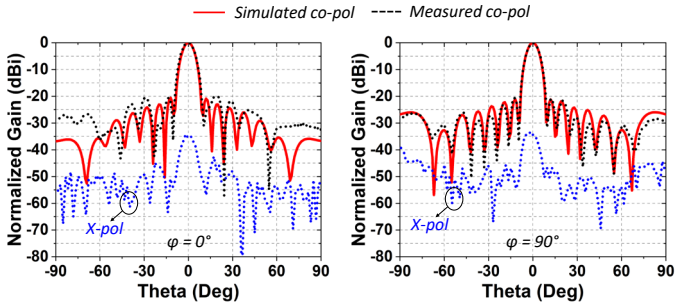

Fig. 14. Measured and simulated normalized realized gain patterns in the two principal vertical planes at 28 GHz.

TABLE I:
PERFORMANCE COMPARISONS OF TYPICAL EXAMPLES OF HIGH GAIN ANTENNA ARRAYS WITH LOW SIDELOBE LEVELS
*(): Simulated result

Ref.	No. of Elements	FBW %	Max SLL Level and Peak Realized Gain (dB)	(dBi)	Peak RAE %
[9]	1 × 8	2.86	-19.7	10.6	~0.18
[10]	6 × 6	6.4	-20.4	18.3	30.8
[11]	3 × 3	1.7	-28.0	12.8	48.0
[12]	1 × 10	~1	-25.3	14.5	~29.6
[13]	2 × 6	1.8	-23.0	16.1	34.4
[14]	8 × 8	16	-18.0	24.0	30.2
[15]	16 × 16	13.8	-25.0	29.5	~58.0
[17]	4 × 4	35.5	-15.6	17.4	~30.2
[18]	4 × 4	5.7	-20.6	17.5	67.0
This Work	**8 × 16**	**10.0 (10.5)**	**-20.0 (-20.0)**	**27.8 (28.0)**	**81.4 (82.0)**

VI. CONCLUSION

A Huygens antenna array with exceptionally high RAE values and low sidelobe levels was reported. To the best of our knowledge and as justified with the comparison Table I of the developed array and recently reported low-sidelobe arrays, it is the first reported array with low sidelobes (less than –20 dB) that achieves a measured peak RAE value higher than 81%. Notably, it is also the first array that has achieved an AE value close to 100% under uniform excitation. Because of its high RAE values, low sidelobe levels, and reasonable bandwidth, the developed Huygens array is an ideal candidate for 5G mm-wave wireless applications requiring high efficiencies and low sidelobe levels.

ACKNOWLEDGEMENTS

The authors would like to thank Prof. G.-L. Huang, Foshan University, for his assistance in the measurements, and Prof. Y. Jay Guo, University of Technology Sydney, for his support of these efforts.

REFERENCES

[1] C. A. Balanis, *Antenna Theory: Analysis and Design*. Hoboken, NJ, USA: Wiley, 2016.

[2] T. S. Rappaport, J. N. Murdock, and F. Gutierrez, "State of the art in 60-GHz integrated circuits and systems for wireless communications," *Proc. IEEE*, vol. 99, no. 8, pp. 1390–1436, Aug. 2011.

[3] J. Teniente, R. Gonzalo, and C. D. Rio, "Low sidelobe corrugated horn antennas for radio telescopes to maximize G/T_s," *IEEE Trans. Antennas Propag.*, vol. 59, no. 6, pp. 1886–1893, June 2011.

[4] D. M. Pozar and B. Kaufman, "Design considerations for low sidelobe microstrip arrays," *IEEE Trans. Antennas Propag.*, vol. 38, no. 8, pp. 1176–1185, Aug. 1990.

[5] J. N. Sahalos, "Design of shared aperture radar arrays with low sidelobe level of the two-way array factor," *IEEE Trans. Antennas Propag.*, vol. 68, no. 7, pp. 5415–5420, July 2020.

[6] T. Y. Yang, W. Hong, and Y. Zhang, "Wideband millimeter-wave substrate integrated waveguide cavity-backed rectangular patch antenna," *IEEE Antennas Wireless Propag. Lett.*, vol. 13, pp. 205–208, 2014.

[7] Y. R. Ding and Y. J. Cheng, "Ku/Ka dual-band dual-polarized shared aperture beam-scanning antenna array with high isolation," *IEEE Trans. Antennas Propag.*, vol. 67, no. 4, pp. 2413–2422, Apr. 2019.

[8] M. S. Sorkherizi, A. Dadgarpour, and A. A. Kishk, "Planar high efficiency antenna array using new printed ridge gap waveguide technology," *IEEE Trans. Antennas Propag.*, vol. 65, no. 7, pp. 3772–3776, Jul. 2017.

[9] F. C. Chen, H. T. Hu, R. S. Li, Q. X. Chu, and M. J. Lancaster, "Design of filtering microstrip antenna array with reduced sidelobe level," *IEEE Trans. Antennas Propag.*, vol. 65, no. 2, pp. 903–908, Feb. 2017.

[10] K. Xing , B. Liu, Z. Guo, X. Wei, R. Zhao, and Y. Ma, "Backlobe and sidelobe suppression of a Q-band patch antenna array by using substrate integrated coaxial line feeding technique," *IEEE Antennas Wireless Propag. Lett.*, vol 16, pp. 3043–3046, 2017.

[11] R. Chopra and G. Kumar, "Series-fed binomial microstrip arrays for extremely low sidelobe level," *IEEE Trans. Antennas Propag.*, vol. 67, no. 6, pp. 4275–4279, Jun. 2019.

[12] J. Yin, Q. Wu, C. Yu, H. Wang and W. Hong, "Low-sidelobe-level series-fed microstrip antenna array of unequal interelement spacing," *IEEE Antennas Wireless Propag. Lett.*, vol. 16, pp. 1695–1698, 2017.

[13] R. Manikandan, P.K. Jawahar and P.H. Rao, "Low sidelobe level CSRR loaded weighted array antenna," *IEEE Trans. Antennas Propag.*, vol. 66, no. 12, pp. 6893–6905, Dec. 2018.

[14] X. Jiang et al., "Ka-band 8 × 8 low-sidelobe slot antenna array using a 1-to-64 high-efficiency network designed by new printed RGW technology," *IEEE Antennas Wireless Propag. Lett.*, vol. 18, no. 6, pp. 1248–1252, Jun. 2019.

[15] G. L. Huang, S. G. Zhou, T. H. Chio, H. T. Hui, and T. S. Yeo "A low profile and low sidelobe wideband slot antenna array fed by an amplitude-tapering waveguide feed-network," *IEEE Trans. Antennas Propag.*, vol. 63, no. 1, pp. 419–423, Jan. 2015.

[16] Y. Geng, J. Wang, Y. Li, Z. Li, M. Chen and Z. Zhang, "High-efficiency leaky-wave antenna array with sidelobe suppression and multibeam generation," *IEEE Antennas Wireless Propag. Lett.*, vol. 16, pp. 2787–2790, 2017.

[17] T. Li and Z. N. Chen, "Wideband sidelobe-level reduced Ka-band metasurface antenna array fed by substrate-integrated gap waveguide using characteristic mode analysis," *IEEE Trans. Antennas Propag.*, vol. 68, no. 3, pp. 1356–1365, Mar. 2020.

[18] W. Lin and R. W. Ziolkowski, "Compact, highly efficient Huygens antenna array with low sidelobe and backlobe levels," *IEEE Trans. Antennas Propag.*, vol. 69, no. 10, pp. 6401-6409, Oct. 2021.

[19] R. W. Ziolkowski, "Using Huygens multipole arrays to realize unidirectional needle-like radiation," *Phys. Rev. X*, vol. 7, 031017, Jul. 2017.

[20] W. Lin and R. W. Ziolkowski, "Theoretical analysis of beam-steerable broadside-radiating Huygens dipole antenna arrays and experimental verification of an ultrathin prototype for wirelessly powered IoT applications," *IEEE Open J. Antennas Propag.*, vol. 2, pp. 954-967, Sep. 2021.

[21] K.-M. Luk and H. Wong, "A new wideband unidirectional antenna element," *Int. J. Microw. Opt. Technol.*, vol. 1, no. 1, pp. 35–44, Jun. 2006.

[22] L. Ge and K.-M. Luk, "A low-profile magneto-electric dipole antenna," *IEEE Trans. Antennas Propag.*, vol. 60, no. 4, pp. 1684–1689, Apr. 2012.

[23] C. A. Balanis, *Advanced Engineering Electromagnetics*, 2nd Ed. Hoboken, N.J.: John Wiley & Sons, 2012.

[24] R. J. Mailloux, *Phased Array Antenna Handbook*, 2nd Ed. Norwood, MA: Artech House, 2005.